Existence of topological nontrivial surface states in strained transition metals: W, Ta, Mo, and Nb

Danny Thonig,[1] Tomáš Rauch,[2] Hossein Mirhosseini,[3,*] Jürgen Henk,[2,†] Ingrid Mertig,[2,3] Henry Wortelen,[4] Bernd Engelkamp,[4] Anke B. Schmidt,[4] and Markus Donath[4]

[1]*Department of Physics and Astronomy, Material Theory, University Uppsala, Box 516, 75120 Uppsala, Sweden*

[2]*Institute of Physics, Martin Luther University Halle-Wittenberg, Von-Seckendorff-Platz 1, 06120 Halle (Saale), Germany*

[3]*Max Planck Institute of Microstructure Physics, Weinberg 2, 06120 Halle (Saale), Germany*

[4]*Physikalisches Institut, Westfälische Wilhelms-Universität, Wilhelm-Klemm-Strasse 10, 48149 Münster, Germany*

(Received 12 May 2016; revised manuscript received 15 July 2016; published 19 October 2016)

We show that a series of transition metals with strained body-centered cubic lattice—W, Ta, Nb, and Mo—hosts surface states that are topologically protected by mirror symmetry and, thus, exhibits nonzero topological invariants. These findings extend the class of topologically nontrivial systems by topological crystalline transition metals. The investigation is based on calculations of the electronic structures and of topological invariants. The signatures of a Dirac-type surface state in W(110), e.g., the linear dispersion and the spin texture, are verified. To further support our prediction, we investigate Ta(110) both theoretically and experimentally by spin-resolved inverse photoemission: unoccupied topologically nontrivial surface states are observed.

DOI: 10.1103/PhysRevB.94.155132

I. INTRODUCTION

Topological insulators have become an exciting topic in condensed matter physics [1]. Insulating in the bulk, these systems host topologically protected surface states that cross the global band gap and exhibit spin-momentum locking. These features render them very valuable for fundamental research and promising for spintronic applications. Up to now, most investigations have addressed strong topological insulators (TIs; in particular strained HgTe [2] as well as Bi_2Te_3 and similar compounds [3]) and topological crystalline insulators (TCIs, e.g., SnTe [4,5]).

Recent experimental investigations of the surface electronic structure of W(110) have brought a remarkable surface state to attention [6–8], followed up by theoretical calculations [9–13]. This surface state is strongly spin polarized due to Rashba spin-orbit coupling [14–16]. But more strikingly, it shows linear and strong dispersion along the $\overline{\Gamma}$-$\overline{H}$ high-symmetry line of the surface Brillouin zone [Fig. 1(a)]. It is therefore reminiscent of a TI's surface state [1,3], although it becomes flattened along $\overline{\Gamma}$-$\overline{N}$ due to the twofold rotational symmetry of the surface.

The salient properties of this surface state immediately raise the question whether it is a "true" topologically nontrivial surface state (TSS) or it is "only" reminiscent of a TSS. In this paper we prove that the surface state of W(110) is indeed topologically protected; this is achieved by calculating the respective topological invariants for slightly strained W bulk (compressed by up to 4% in the calculations). On top of this, we show that it has analogs in other transition metals with body-centered-cubic (bcc) lattice: Ta, Nb, and Mo. We provide both experimental and theoretical evidence for the exemplary material Ta. Having identified a number of transition metals hosting TSSs, our findings call for investigating other material classes—besides insulators and semimetals [17–23]—that may host topologically protected edge states. Recently, Au(111) with increased strength of the spin-orbit coupling has been identified topologically nontrivial [24].

The paper is organized as follows. In Sec. II we present the theoretical and experimental methods used to describe topological nontrivial surface states. Results and discussions are presented in Sec. III. Finally, we give conclusions in Sec. IV. Further details are given in the Appendixes.

II. METHODS

Ab initio electronic-structure calculations for both bulk and (110) surfaces of W, Ta, Nb, and Mo have been performed within the local density approximation to density-functional theory (DFT), using Perdew-Burke-Ernzerhof generalized gradient exchange-correlation functionals [25,26] and two independent methods: Korringa-Kohn-Rostoker and VASP. Experimental investigations of the unoccupied states of Ta(110) were performed by spin- and angle-resolved inverse photoemission.

A. Korringa-Kohn-Rostoker calculations

We have applied relativistic multiple-scattering theory as formulated in the Korringa-Kohn-Rostoker (KKR) approach [27,28] that is based on multiple-scattering theory [29]. Solving the Dirac equation, relativistic effects are fully accounted for, especially the spin-orbit interaction which is essential for heavy elements such as Ta and W. Finite-size effects are excluded by modeling the surfaces in a semi-infinite geometry. The computations have been performed with the OMNI program package [30] which is an implementation of the layer-KKR scheme [27]; this approach is well suited for semi-infinite systems (e.g., surfaces and interfaces).

The spectral density $n_{i\alpha}(E,\boldsymbol{k}_\parallel)$, i.e., the energy- and wave-vector-resolved local density of states for a site α in layer i, is computed from the site-resolved Green function $G_{i\alpha,i\alpha}(E+i\eta,\boldsymbol{k}_\parallel)$,

$$n_{i\alpha}(E,\boldsymbol{k}_\parallel) = -\frac{1}{\pi}\,\mathrm{Im}\,\mathrm{Tr}\,G_{i\alpha,i\alpha}(E+i\eta,\boldsymbol{k}_\parallel). \qquad (1)$$

*Present address: Max Planck Institute for Chemical Physics of Solids, Nöthnitzer Str. 40, 01187 Dresden, Germany.

†Corresponding author: juergen.henk@physik.uni-halle.de

 ©2016 American Physical Society

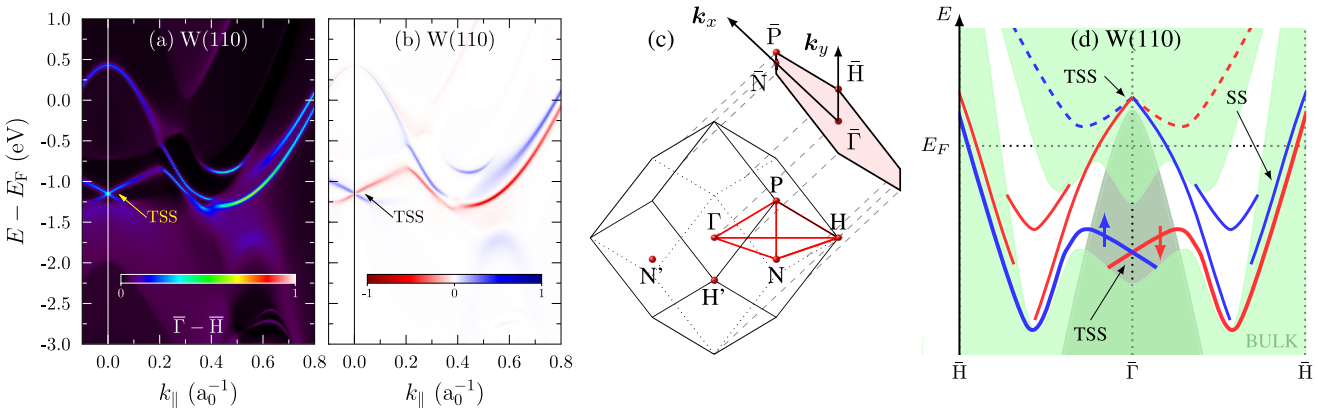

FIG. 1. Surface electronic structure of W(110). (a) Topological surface state (marked TSS). The spectral density of the topmost layers is shown as normalized color scale for the $\bar{\Gamma}$-$\bar{H}$ line of the surface Brillouin zone. (b) As (a), but spin resolved with respect to the Rashba component of the spin polarization (± 1 is fully spin polarized: -1 spin-down, $+1$ spin-up). (c) Brillouin zone of a bcc lattice and its projection onto the (110) surface. Red lines indicate an irreducible part. H and H' become inequivalent under strain. (d) Schematic illustration of the surface-state dispersion from (a), with spin polarization indicated by colors. Recall that bulk states show up also in the dark green area around $\bar{\Gamma}$ because they are projected onto the surface Brillouin zone.

η is a small offset from the energy axis leading to a broadening of the spectral density; typically $\eta \approx 0.01$ eV. The spectral density can further be decomposed with respect to spin polarization and angular momentum, thus allowing for a detailed characterization of the electronic states.

B. VASP calculations

The KKR calculations are complemented by analogous computations with the VASP program package [31,32], using a slab geometry. The Vienna *ab initio* simulation package (VASP) solves the Kohn-Sham equations by augmented plane waves basis sets [31,32]; this allows us to treat the full crystal potential and, consequently, structural relaxations. Relativistic effects are accounted for by first-order perturbation in the spin-orbit coupling which requires handling of the core states by projector-augmented-wave pseudopotentials (PAW) [33,34]. The Perdew-Burke-Ernzerhof generalized gradient approximation (PBE-GGA) for the exchange correlation avoids side effects from strongly varying charge densities in W, Ta, Nb, and Mo. To mimic (110) surfaces, we utilized slabs 15 layers thick in which relaxations are allowed in the first 8 layers. The vacuum region is chosen as wide as 27 bulk interlayer distances.

The reciprocal space is partitioned using a Monkhorst mesh with $21 \times 21 \times 21$ and $21 \times 21 \times 1$ points for bulk and slab calculations, respectively. Plane wave expansions in the valence-band region are cutoff at 520 eV.

The electronic structures obtained by the VASP and KKR methods agree very well, putting our findings on firm ground.

C. Surface relaxations

Surface relaxations have been determined by VASP calculations (Table I; to obtain optimal structural relaxations, we utilized a Methfessel-Paxton smearing of the order 2 with a broadening of 0.05 eV). They are important ingredients in our reasoning.

Experimental lattice parameters for W(110) agree with the theoretical predictions: Ref. [37] gives $d_{12} = -2.2 \pm 1.0\%$, whereas Ref. [38] states $d_{12} = -2.7(5)\%$ and $d_{23} < 0.3\%$. The calculated layer relaxations agree with those of previous theoretical studies: for Mo(110) [39–42], for Nb(110) [43], and for Ta(110) [44].

D. Tight-binding calculations

The DFT results serve as input for tight-binding (TB) parametrizations for W, Ta, Nb, and Mo, from which we calculate Berry curvatures and mirror Chern numbers n_m.

The TB calculations for bcc W, Ta, Nb, and Mo rely on the Slater-Koster parametrization [45] including spin-orbit coupling; the TB parameter are listed in Appendix A. First- and second-nearest-neighbor parameters have been considered. For the distorted systems, the TB parameters have been scaled according to Harrison [46].

For the surface electronic structure, we have applied Green function renormalization which treats semi-infinite systems accurately [47,48]. This approach yields the spectral density, see Eq. (1).

The tight-binding approach proved successful for, e.g., Bi_2Te_3, Bi_2Se_3, SnTe, and $HgTe_xS_{1-x}$ [49–51]. Recall that

TABLE I. Geometry of bcc(110) surfaces obtained from VASP calculations. The relative changes of the distances d_{ij} between layer i and j is given with respect to the bulk interlayer distance; $i, j = 1,2,3,\ldots$ indicate the topmost, second, third layer, etc., a is the lattice constant. Data for Ta reproduced from [35,36].

	W	Ta	Mo	Nb
d_{12}	-3.67%	-4.81%	-4.96%	-3.77%
d_{23}	$+0.92\%$	$+0.57\%$	$+1.32\%$	$+1.19\%$
d_{34}	$+0.20\%$	$+0.29\%$	$+0.41\%$	$+0.11\%$
a	3.172 Å	3.308 Å	3.151 Å	3.323 Å

our TB and DFT calculations are in good agreement (Appendix A).

E. Mirror Chern numbers

A mirror Chern number classifies systems in which the topological protection is brought about by mirror symmetry in the bulk (topological crystalline insulators, TCIs). We consider mirror planes which are perpendicular to the (110) surface and cut the $\overline{\Gamma}$-$\overline{H}$ and $\overline{\Gamma}$-$\overline{N}$ lines of the surface Brillouin zone [Fig. 1(c)]. The modulus of n_{m} equals the number of TSSs for the respective mirror plane, its sign determines the spin chirality of these TSSs.

The mirror Chern number n_{m} of the N lowest bands is defined as [52]

$$n_{\mathrm{m}} = \tfrac{1}{2}(n_{+i} - n_{-i}), \tag{2}$$

with

$$n_{\pm i} = \int \boldsymbol{\Omega}_{\pm i}(\boldsymbol{k}) \cdot \boldsymbol{e}_n \, d^2k, \tag{3}$$

the Chern number of the $N/2$ states with mirror eigenvalue of $\pm i$. $\boldsymbol{e}_n$ is a unit vector normal to the mirror plane and

$$\boldsymbol{\Omega}_{\pm i}(\boldsymbol{k}) = i \sum_{n=1}^{\frac{N}{2}} \left\langle \nabla_{\boldsymbol{k}} u_n^{\pm i}(\boldsymbol{k}) \right| \times \left| \nabla_{\boldsymbol{k}} u_n^{\pm i}(\boldsymbol{k}) \right\rangle \tag{4}$$

is the sum of the Berry curvatures of all these $N/2$ bands. $u_n^{\pm i}(\boldsymbol{k})$ is the periodic part of the nth Bloch function with mirror eigenvalue $\pm i$. The integration in Eq. (3) is over the intersection of the mirror plane with the bulk Brillouin zone.

If $n_{\mathrm{m}} \neq 0$, the bulk-boundary correspondence [1] tells there have to be $|n_{\mathrm{m}}|$ surface states connecting the Nth with the $(N+1)$th bulk band. These surface states are located at the projection of the mirror plane onto the surface Brillouin zone.

F. Inverse-photoemission experiments

The Ta(110) surface was cleaned by repeated cycles of heating. Prolonged heating in an oxygen atmosphere of 6×10^{-8} mbar at temperatures of 1800 K was followed by short-time heating to temperatures of 2700 K. These high temperatures were necessary to dissolve the strong surface interaction with oxygen. The cleaning procedure was effective to remove contaminants, such as C and O, from the surface. The surface quality was confirmed by Auger electron spectra and by a (1×1) low-energy electron diffraction pattern with sharp diffraction spots and low background intensity. Photoemission data of the occupied surface state just below the Fermi level served as an additional sensitive criterion for a clean surface. For details see Refs. [35,53].

The experimental setup is depicted in Fig. 2. The sample was irradiated with spin-polarized electrons of defined energy and momentum, given by the angle of incidence θ with respect to the surface normal $\boldsymbol{n}$. The electrons are photoexcited from a GaAs cathode in our rotatable spin-polarized electron source ROSE [54]. The spin-polarization direction of the impinging electrons was adjusted perpendicular to their in-plane wave vector $\boldsymbol{k}_{\parallel}$ and perpendicular to the surface normal $\boldsymbol{n}$, i.e., being sensitive to the Rashba component. The azimuth of the sample can be adjusted by varying the angle Φ. The emitted photons

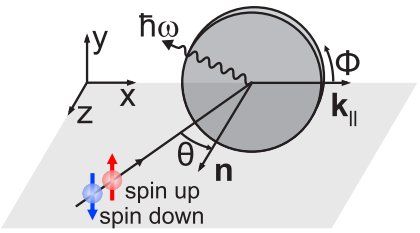

FIG. 2. Geometry for the spin- and angle-resolved inverse-photoemission experiments.

($\hbar\omega = 9.9$ eV) were detected at an angle of 65° relative to the electron beam in the plane of incidence and 32° perpendicular to it. More information about the experiment is given in Refs. [35,55].

III. RESULTS AND DISCUSSION

A. Semimetal band gap and band inversion

Since the Dirac-type surface state of W(110) has been investigated in every detail [6,7,11,13,56,57], we provide experimental evidence for TSSs in Ta(110). For this purpose we used spin- and angle-resolved inverse photoemission (IPE). The spin-dependent unoccupied electronic structure of Ta(110) was investigated by utilizing a spin-polarized electron beam [54] and measuring the Rashba component of the spin polarization (for details, see Sec. II F).

Topologically nontrivial systems are characterized by band inversions which give rise to nonzero topological invariants; the latter are defined for and computed from the bulk states. If the system exhibits either a global or a semimetal gap [58] the invariant is integer, which is obviously the case for insulators. Focusing first on W(110), we are facing two problems: semimetal band gap and band inversion.

Semimetal band gap. Bulk W does not have a band gap in the energy region in which the relevant surface state shows up [Figs. 1(a) and 3(a)]. However, both compressive or tensile strain in [110] direction open up the desired semimetal gap in the $\overline{\Gamma}$-$\overline{H}$ and $\overline{\Gamma}$-$\overline{N}$ mirror planes, thus allowing us to compute the mirror Chern numbers n_{m}. We have applied strain up to $\pm 4\%$ which is in the range of the surface relaxation (Table I) and would like to emphasize that any nonzero strain breaks the point-group symmetry and causes the opening of a gap. Such a strain could be studied by growing metal films on, e.g., a piezocrystal [59].

Band inversion. Although the Dirac-type surface state is observed at the $\overline{\Gamma}$ point of the surface Brillouin zone, the relevant band inversion takes place at the H points of the bulk Brillouin zone (Fig. 3), i.e., at energies larger than the Fermi level E_{F}. The "small group" of H is O_h and the six t_{2g} bulk bands are split into one twofold degenerate $E_{5/2g}$ and one fourfold degenerate $G_{3/2g}$ level if spin-orbit coupling is considered. Under strain along [110], the small group of H is reduced to D_{2h}. The $E_{5/2g}$ level stays twofold degenerate, the $G_{3/2g}$ level is further split into two twofold degenerate levels. All these levels belong to the representation $E_{1/2g}$. This splitting shows up for both tensile and compressive strain and is observed in TB as well as KKR (cf. Appendix B).

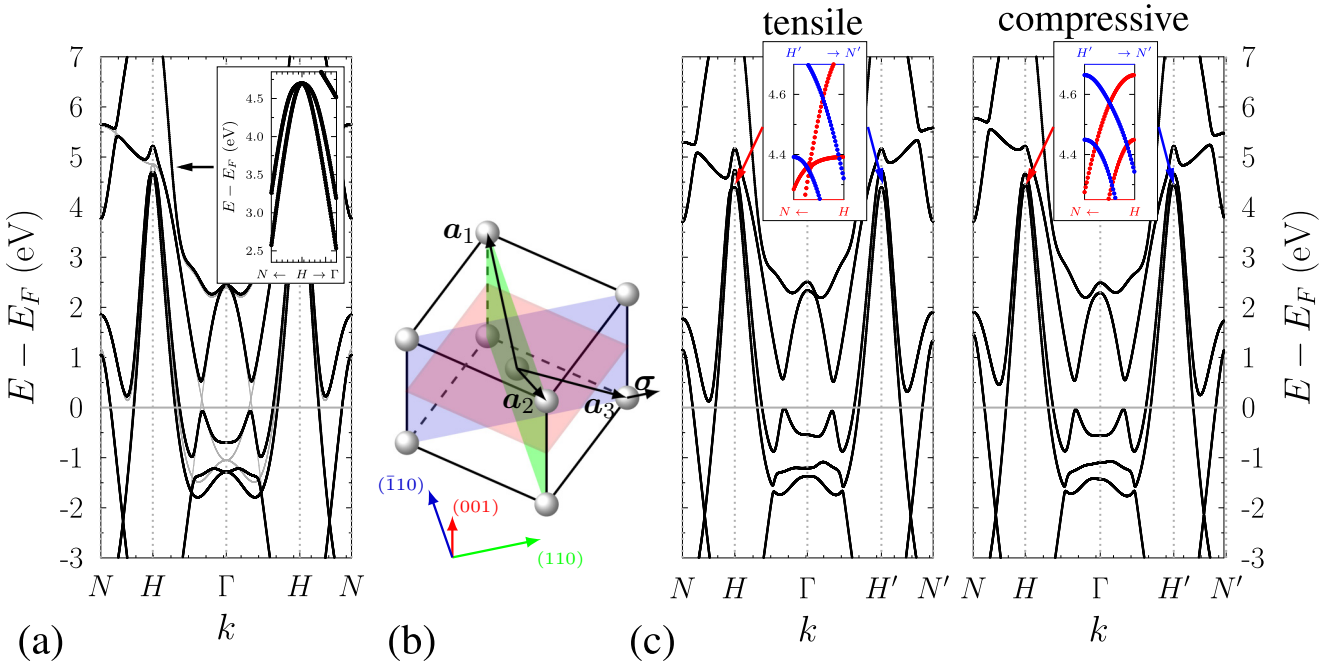

FIG. 3. Band inversion and band gap opening in W. Tight-binding band structures are shown along those lines in the bulk Brillouin zone that are relevant for the topological phase transition. (a) Cubic W without (gray) and with (black) spin-orbit coupling. The inset shows a zoom to the topological "hot spot" of the dispersion (b) body-centered cubic crystal, with lattice sites represented by spheres; the green area visualizes the unit cell of the (110) surface spanned by the lattice vectors $\boldsymbol{a}_1$ and $\boldsymbol{a}_2$. The lattice vector between the (110) planes is $\boldsymbol{a}_3$ which is altered upon strain $\boldsymbol{\sigma}$. The two mirror planes—with surface normal in (001) and ($\bar{1}$10)—for which the Chern numbers have been computed are displayed in blue and red. (c) Tensile and compressively strained W with spin-orbit coupling. Insets show band dispersions that are relevant for the topology of W under strain at H (red) and H' (blue). H' and N' are defined in Fig. 1(c).

For the strained bulk systems with semimetal band gaps we compute the mirror Chern numbers n_m for both the $\overline{\Gamma}$-$\overline{H}$ and $\overline{\Gamma}$-$\overline{N}$ mirror planes. For tensile strain we find $n_\mathrm{m} = 0$, indicating a topological trivial system. For compressive strain, n_m for the $\overline{\Gamma}$-$\overline{N}$ mirror plane vanishes as well; we recall that the surface state is weakly dispersive along this line [7]. However, for the $\overline{\Gamma}$-$\overline{H}$ mirror plane—for which the surface state shows linear dispersion—we compute $n_\mathrm{m} = -2$. The results of our calculations are summarized in Table II. This finding indicates that compressively strained W is a metal hosting TSSs in the semimetal gap. It further tells us that the semimetal band gap has to be bridged by two TSSs with identical spin chirality. Analogous calculations for Ta, Mo, and Nb give identical results concerning the topological properties. Recall that in W and Mo the TSSs are occupied while in Ta and Nb they are unoccupied.

To provide qualitative insight into the complicated electronic structure we turn to Ta(110) [Fig. 4(a)]. In the TB calculations for the surface we assume homogeneously strained samples (i.e., without detailed surface relaxation) and bulk TB parameters in the topmost layers. By calculating the bulk band structure along $\overline{\Gamma}$-$\overline{H}$–$\overline{N}$ for a set of equidistant $k_\perp$, we achieve a representation of the $(E,\boldsymbol{k})$-dependent semimetal band gap: the band that forms its lower (upper) boundary is colored green (red). This band structure is superimposed onto the surface spectral density which shows two surface states. The surface state TSS1 starts at 1.0 eV at $\overline{\Gamma}$ off a green bulk band and can be traced to $\overline{H}$ where it snuggles up to bulk band edge; then it disperses to higher energies at $\overline{N}$ where it connects to a red bulk band. TSS2 starts at 1.45 eV at $\overline{\Gamma}$ off a red band and reaches a green bulk band close to $\overline{H}$. The spin-resolved spectral density tells that TSS1 and TSS2 have opposite spin polarization [Fig. 4(b)]. Note that TSS1 (TSS2) exhibits its part above (below) its Dirac point at $\overline{\Gamma}$ which has opposite spin polarization as compared to its lower (upper) part [cf. Figs. 1(b) and 1(d) for W]. The spin chirality of TSS1 and TSS2 is therefore identical, which is in line with the mirror Chern number $n_\mathrm{m} = -2$.

TABLE II. Mirror Chern numbers n_m of the $\overline{\Gamma}$-$\overline{H}$ and the $\overline{\Gamma}$-$\overline{N}$ plane calculated for both compressive and tensile strain.

	$\overline{\Gamma}$-$\overline{H}$	$\overline{\Gamma}$-$\overline{N}$
Tensile	0	0
Compressive	−2	0

B. Topological surface states in Ta(110), Mo(110), and Nb(110)

We now show by *ab initio* calculations and IPE experiments that Ta(110) (cf. Appendix C) also hosts TSSs. Ta lends itself for an investigation because its strong spin-orbit coupling produces a sizable spin-orbit band gap. The semimetal gap is between the dispersive bands that become inverted by compressive strain (cf. Fig. 7). Near $\overline{\Gamma}$ it shows up at $E_\mathrm{F} + 1.1$ eV [Fig. 4(c)]. Two surface bands with opposite spin polarization are split off the bulk band edges at $\overline{\Gamma}$, one from the lower, the other from the upper band edge, in accordance

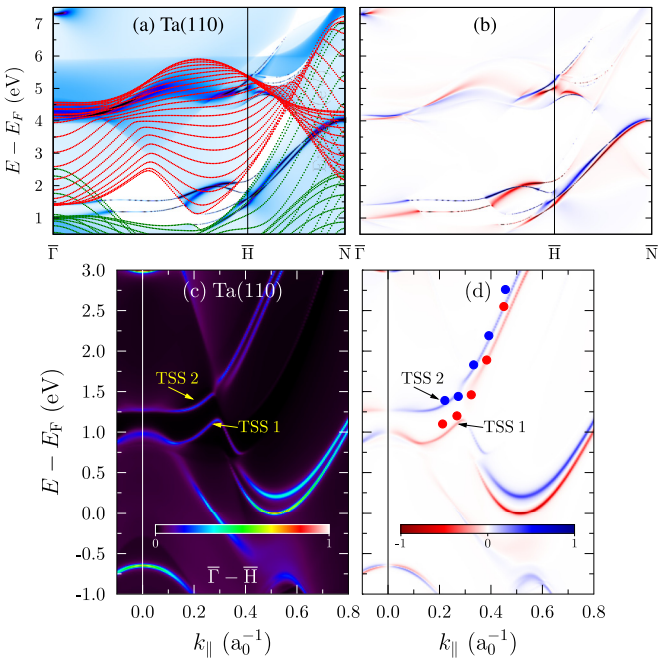

FIG. 4. Unoccupied electronic structure of Ta(110) for the $\overline{\Gamma}$-$\overline{H}$ line of the surface Brillouin zone. (a) Spectral density of the topmost surface layer of unstrained Ta calculated with the tight-binding method. The bulk bands that form the boundary of the (E,$\boldsymbol{k}$)-dependent band gap are shown in green and red. (b) As (a) but resolved with respect to the Rashba spin component. (c) and (d) As (a) and (b) but calculated by the *ab initio* KKR method. The symbols result from spin-resolved inverse-photoemission experiments and indicate peak positions derived from spectra shown in Fig. 8. The topological surface states are marked TSS1 and TSS2.

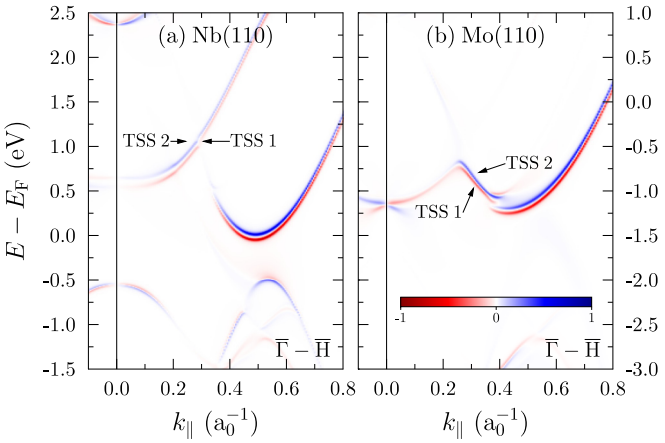

FIG. 5. Spin-resolved surface electronic structure of Nb(110) (a) and Mo(110) (b), analogous to Fig. 4(d).

with $n_m = -2$ [Figs. 4(c) and 4(d) as well as Fig. 1(d)]. The two TSSs do not exhibit the typical Rashba-type dispersion, as observed in Au(111) and Bi/Ag(111) [60–62]. Along the $\overline{\Gamma}$-$\overline{H}$ line they disperse in "unison" with nonlinear dispersion [63]. Surface bands appear at lower energies relative to the bulk band edges than those of W, which is attributed to the larger lattice constant a and the stronger surface relaxation of Ta compared to W (Table I). An increased lattice constant "flattens" the bulk bands, resulting in downshifted surface bands and stronger hybridizations with the bulk states. Since the TSS in W(110) is located at the lower boundary of the band gap at $\overline{\Gamma}$ (about -1.25 to -0.75 eV in Fig. 1(a) [11]), the respective Ta surface state and its Dirac point are "hidden" in the bulk bands at $\overline{\Gamma}$ [64,65].

Strained Ta, Nb, and Mo possess the same topological invariants as W. Both Nb and Mo host TSSs as well (Fig. 5; cf. Ref. [40] for Mo). Since both Nb ($Z = 41$, $4d^4 5s^1$) and Mo ($Z = 42$, $4d^5 5s^1$) are lighter than Ta ($Z = 73$, $5d^3 6s^2$) and W ($Z = 74$, $5d^4 6s^2$) the band gaps induced by the spin-orbit interaction are significantly smaller. The surface state in Mo resembles a Dirac-like state at $\overline{\Gamma}$ and $E - E_F = -1.2$ eV; the dispersion is not linear, in agreement with experiment [66,67]. The orbital composition of the surface states is similar to those in Ta(110) and W(110).

IV. CONCLUSION

In summary, we showed that the transition metals W, Ta, Nb, and Mo host topologically protected surface states. Nonzero compressive strain opens an inverted band gap at the H point of the bulk Brillouin zone which causes nonzero topological invariants (mirror Chern numbers $n_m = -2$). These findings indicate the existence of topological surface states with identical spin polarization at the (110) surfaces. Since the (110) surfaces are effectively compressed (Table I), the four considered bcc metals appear topologically nontrivial although their bulk lattice is cubic.

To further confirm the predictions for Nb and Mo, we encourage investigations of their electronic structure by spin-resolved conventional or inverse photoemission. The topological phase transition upon strain could be studied by growing metal films on either different substrates, on a piezocrystal [59,68], or by bending the sample; strain in the bulk then would show up in addition to the already effectively compressed surface. Other surfaces are worth investigating as well.

ACKNOWLEDGMENTS

We acknowledge fruitful discussions with Albert Fert. This work is supported by the Priority Program SPP 1666 of DFG.

APPENDIX A: TIGHT-BINDING PARAMETERS

The tight-binding parameters for bcc W, Ta, Nb, and Mo (Table III) have been obtained by fitting the bulk band structures of the *ab initio* KKR calculations using a Monte Carlo approach, with focusing on agreement in the energy region of the topologically nontrivial surface states. The agreement of the TB and the DFT band structure is visualized for W in Fig. 6.

APPENDIX B: STRAIN IN [110] DIRECTION AND BAND INVERSION

Topological invariants are defined for groups of bands that are separated by band gaps. More precisely, to calculate the mirror Chern number n_m for the lowest N bands, there has to

TABLE III. Slater-Koster tight-binding parameters for W, Ta, Nb, and Mo in units of eV. E_s, E_p, E_d, λ_p, and λ_d stand for the on-site energies and spin-orbit coupling constants, respectively. The subscripts indicate the neighbors' order (1 for first- and 2 for second-nearest neighbors.)

	W	Ta	Mo	Nb
E_s	12.532	11.232	14.997	12.741
E_p	17.839	16.648	18.517	16.223
E_d	7.964	8.140	7.400	7.083
λ_p	0.86	0.65	0.24	0.19
λ_d	0.18	0.137	0.05	0.043
$(ss\sigma)_1$	− 1.574	− 1.405	− 1.623	− 1.455
$(sp\sigma)_1$	2.486	2.414	2.226	− 2.105
$(sd\sigma)_1$	− 1.582	− 1.542	1.035	1.251
$(pp\sigma)_1$	2.429	2.270	2.495	2.260
$(pp\pi)_1$	− 0.536	− 0.539	− 0.535	− 0.503
$(pd\sigma)_1$	− 2.188	− 2.128	1.874	− 1.768
$(pd\pi)_1$	0.028	0.068	0.009	− 0.032
$(dd\sigma)_1$	− 1.573	− 1.561	− 1.404	− 1.386
$(dd\pi)_1$	0.743	0.731	0.666	0.657
$(dd\delta)_1$	− 0.023	− 0.048	− 0.052	− 0.007
$(ss\sigma)_2$	− 0.291	− 0.302	− 0.355	− 0.203
$(sp\sigma)_2$	0.508	0.361	0.681	− 0.580
$(sd\sigma)_2$	− 0.831	− 0.563	1.018	0.738
$(pp\sigma)_2$	0.891	0.857	1.006	0.936
$(pp\pi)_2$	− 0.056	− 0.066	− 0.043	− 0.114
$(pd\sigma)_2$	− 1.613	− 1.649	1.546	− 1.481
$(pd\pi)_2$	0.247	0.242	− 0.374	0.227
$(dd\sigma)_2$	− 0.908	− 0.838	− 0.739	− 0.852
$(dd\pi)_2$	0.188	0.245	0.280	0.223
$(dd\delta)_2$	0.086	− 0.007	0.006	0.080

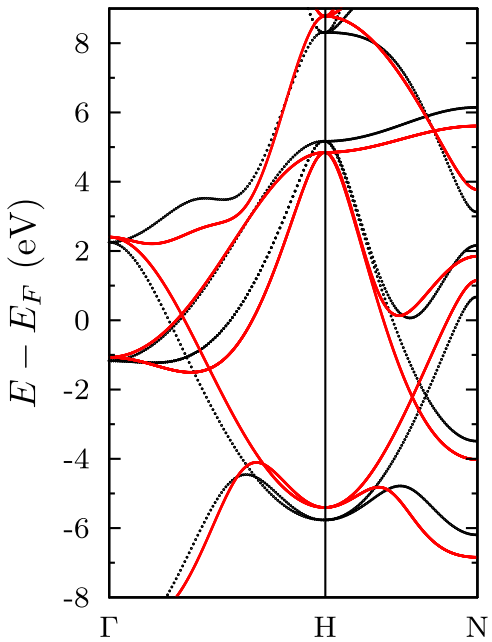

FIG. 6. Bulk band structure of cubic W without spin-orbit coupling calculated with VASP (black) and with the tight-binding approach (red). E_F is the Fermi energy.

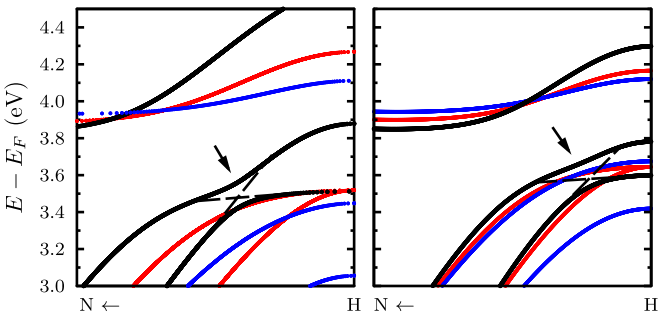

FIG. 7. Bulk band inversion in W, obtained from KKR (left panel) and TB (right panel). The band inversion is mediated by strain of −3% (compressive strain; black line), 0% (red line), and +3% (tensile strain; blue line). Arrows and dashed lines indicate the band gap inversion associated with compressive strain.

be a finite gap between the Nth and $(N+1)$th band for all wave vectors in the considered mirror plane.

In the case of W, the Dirac-type surface state shows up in the local gap at $\overline{\Gamma}$, which opens up between bands 6 and 7, both of which belong to t_{2g} orbitals. Considering both mirror planes ($\overline{\Gamma}$-$\overline{H}$ and $\overline{\Gamma}$-$\overline{N}$), one finds that this gap closes at the H point, ending in a fourfold degenerate level. Lowering the symmetry by applying strain in [110] direction, this fourfold degenerate level splits into two twofold degenerate ones. For both compressive and tensile strain, bands 6 and 7 remain

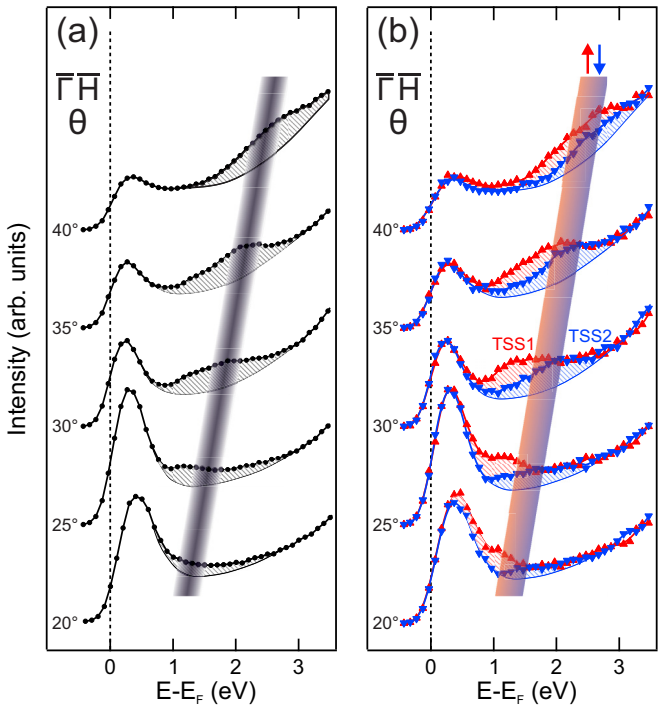

FIG. 8. Spin-integrated (a) and spin-resolved (b) IPE spectra for Ta(110) for various angles of incidence θ in the $\overline{\Gamma}\,\overline{H}$ mirror-symmetry direction. In (b), spin-up (spin-down) is marked by red (blue) triangles. The shape of the background intensity is indicated by solid lines below the surface-state emissions. The precise procedure for determining the energy positions of TSS1 and TSS2 is described in detail in Ref. [35].

separated in the entire $\overline{\Gamma}$-$\overline{H}$ and $\overline{\Gamma}$-$\overline{N}$ mirror planes, allowing us to calculate n_m for both planes.

To further support the TB approach, we compare the KKR with the TB electronic structure in the vicinity of the H point of the bulk Brillouin zone (Fig. 7). We applied 3% of tensile and compressive strain in [110] direction. For the strained systems a band gap opens up at H: the degeneracy of the bands of the cubic system (red) is lifted for the strained systems (black and blue). But only compressive strain leads to a band inversion: due to spin-orbit coupling a band crossing is avoided, as is indicated by dashed lines and arrows. This band inversion is the origin for nonzero mirror Chern numbers in W, Ta, Mo, and Nb.

APPENDIX C: IPE SPECTRA FOR TA(110)

Spin-integrated and spin-resolved IPE spectra along $\overline{\Gamma}\,\overline{H}$ are shown in Fig. 8 for θ between 20° and 40°. They reveal the dispersion and spin texture of TSS1 and TSS2. For determining of the $E(k_\parallel)$ dispersion, the nearby bulk-band edge has to be taken into account. Therefore, the spectra were decomposed into a spin-polarized surface and a spin-independent bulk contribution on top of a spin-independent background intensity. For details, see Ref. [35]. The results of this fitting routine are included as red (TSS1) and blue dots (TSS2) in Fig. 4(d) of the paper in direct comparison with the calculated energy dispersion.

[1] M. Z. Hasan and C. L. Kane, Rev. Mod. Phys. **82**, 3045 (2010).
[2] M. König, S. Wiedmann, C. Brüne, A. Roth, H. Buhmann, L. W. Molenkamp, X.-L. Qi, and S.-C. Zhang, Science **318**, 766 (2007).
[3] M. Z. Hasan and J. E. Moore, Annu. Rev. Condens. Matter Phys. **2**, 55 (2011).
[4] L. Fu, Phys. Rev. Lett. **106**, 106802 (2011).
[5] S.-Y. Xu, C. Liu, N. Alidoust, M. Neupane, D. Qian, I. Belopolski, J. D. Denlinger, Y. J. Wang, H. Lin, L. A. Wray, G. Landolt, B. Slomski, J. H. Dil, A. Marcinkova, E. Morosan, Q. Gibson, R. Sankar, F. C. Chou, R. J. Cava, A. Bansil, and M. Z. Hasan, Nature Commun. **3**, 1192 (2012).
[6] K. Miyamoto, A. Kimura, K. Kuroda, T. Okuda, K. Shimada, H. Namatame, M. Taniguchi, and M. Donath, Phys. Rev. Lett. **108**, 066808 (2012).
[7] K. Miyamoto, A. Kimura, T. Okuda, K. Shimada, H. Iwasawa, H. Hayashi, H. Namatame, M. Taniguchi, and M. Donath, Phys. Rev. B **86**, 161411(R) (2012).
[8] M. Hochstrasser, J. G. Tobin, E. Rotenberg, and S. D. Kevan, Phys. Rev. Lett. **89**, 216802 (2002).
[9] A. G. Rybkin, E. E. Krasovskii, D. Marchenko, E. V. Chulkov, A. Varykhalov, O. Rader, and A. M. Shikin, Phys. Rev. B **86**, 035117 (2012).
[10] F. Giebels, H. Gollisch, and R. Feder, Phys. Rev. B **87**, 035124 (2013).
[11] H. Mirhosseini, M. Flieger, and J. Henk, New J. Phys. **15**, 033019 (2013).
[12] H. Mirhosseini, F. Giebels, H. Gollisch, J. Henk, and R. Feder, New J. Phys. **15**, 095017 (2013).
[13] J. Braun, K. Miyamoto, A. Kimura, T. Okuda, M. Donath, H. Ebert, and J. Minár, New J. Phys. **16**, 015005 (2014).
[14] Y. A. Bychkov and E. I. Rashba, J. Phys. C **17**, 6039 (1984).
[15] Yu. A. Bychkov and È. I. Rashba, Pis'ma Zh. Eksp. Teor. Fiz. **39**, 66 (1984) [JETP Lett. **39**, 78 (1984)].
[16] R. Winkler, *Spin-Orbit Coupling Effects in Two-Dimensional Electron and Hole Systems* (Springer, Berlin, 2003).
[17] S. V. Eremeev, G. Landolt, T. V. Menshchikova, B. Slomski, Y. M. Koroteev, Z. S. Aliev, M. B. Babanly, J. Henk, A. Ernst, L. Patthey, A. Eich, A. A. Khajetoorians, J. Hagemeister, O. Pietzsch, J. Wiebe, R. Wiesendanger, P. M. Echenique, S. S. Tsirkin, I. R. Amiraslanov, J. H. Dil, and E. V. Chulkov, Nat. Commun. **3**, 635 (2012).
[18] M. Bianchi, D. Guan, S. Bao, J. Mi, B. B. Iversen, P. D. C. King, and P. Hofmann, Nat. Commun. **1**, 128 (2010).
[19] L. X. Yang, Z. K. Liu, Y. Sun, H. Peng, H. F. Yang, T. Zhang, B. Zhou, Y. Zhang, Y. F. Guo, M. Rahn, D. Prabhakaran, Z. Hussain, S. K. Mo, C. Felser, B. Yan, and Y. L. Chen, Nat. Phys. **11**, 728 (2015).
[20] Y. Wang, P. Deorani, K. Banerjee, N. Koirala, M. Brahlek, S. Oh, and H. Yang, Phys. Rev. Lett. **114**, 257202 (2015).
[21] Y. Sun, S.-C. Wu, and B. Yan, Phys. Rev. B **92**, 115428 (2015).
[22] B. Yan, M. Jansen, and C. Felser, Nat. Phy. **9**, 709 (2013).
[23] G. Li, B. Yan, R. Thomale, and W. Hanke, Sci. Rep. **5**, 10435 (2015).
[24] B. Yan, B. Stadtmüller, N. Haag, S. Jakobs, J. Seidel, D. Jungkenn, S. Mathias, M. Cinchetti, M. Aeschlimann, and C. Felser, Nat. Commun. **6**, 10167 (2015).
[25] J. P. Perdew, K. Burke, and M. Ernzerhof, Phys. Rev. Lett. **77**, 3865 (1996).
[26] P. Perdew, K. Burke, and M. Ernzerhof, Phys. Rev. Lett. **78**, 1396 (1997).
[27] J. Henk, in *Handbook of Thin Film Materials*, Vol. 2, edited by H. S. Nalwa (Academic, San Diego, 2002), Chap. 10, p. 479.
[28] J. Zabloudil, R. Hammerling, L. Szunyogh, and P. Weinberger, Eds., *Electron Scattering in Solid Matter* (Springer, Berlin, 2005).
[29] P. Weinberger, *Electron Scattering Theory of Ordered and Disordered Matter* (Clarendon, Oxford, 1990).
[30] J. Henk, H. Mirhosseini, P. Bose, K. Saha, N. Fomynikh, T. Scheunemann, S. V. Halilov, E. Tamura, and R. Feder, OMNI—Fully relativistic electron spectroscopy calculations (2009). This source code is available from the authors (J.H.).
[31] G. Kresse and J. Furthmüller, Comput. Mater. Sci. **6**, 15 (1996).
[32] G. Kresse and J. Furthmüller, Phys. Rev. B **54**, 11169 (1996).
[33] P. E. Blöchl, Phys. Rev. B **50**, 17953 (1994).
[34] G. Kresse and D. Joubert, Phys. Rev. B **59**, 1758 (1999).
[35] B. Engelkamp, H. Wortelen, H. Mirhosseini, A. B. Schmidt, D. Thonig, J. Henk, and M. Donath, Phys. Rev. B **92**, 085401 (2015).
[36] H. Wortelen, K. Miyamoto, H. Mirhosseini, T. Okuda, A. Kimura, D. Thonig, J. Henk, and M. Donath, Phys. Rev. B **92**, 161408(R) (2015).
[37] D. Venus, S. Cool, and M. Plihal, Surf. Sci. **446**, 199 (2000).
[38] H. L. Meyerheim, D. Sander, R. Popescu, P. Steadman, S. Ferrer, and J. Kirschner, Surf. Sci. **475**, 103 (2001).
[39] K. Jeong, R. H. Gaylord, and S. D. Kevan, Phys. Rev. B **38**, 10302 (1988).

[40] E. Rotenberg, J. W. Chung, and S. D. Kevan, Phys. Rev. Lett. **82**, 4066 (1999).
[41] K. Kośmider, A. Krupski, P. Jelínek, and L. Jurczyszyn, Phys. Rev. B **80**, 115424 (2009).
[42] F. Zhou and V. Ozoliņš, Phys. Rev. B **80**, 125127 (2009).
[43] K. I. Shein, I. R. Shein, N. I. Medvedeva, E. V. Shalaeva, M. V. Kuznetsov, and A. L. Ivanovskii, Phys. Metals Metallogr. **102**, 604 (2006).
[44] C. J. Wu, L. H. Yang, J. E. Klepeis, and C. Mailhiot, Phys. Rev. B **52**, 11784 (1995).
[45] J. C. Slater and G. F. Koster, Phys. Rev. **94**, 1498 (1954).
[46] W. A. Harrison, *Elementary Electronic Structure*, revised ed. (World Scientific, New Jersey, 2004).
[47] J. Henk and W. Schattke, Comput. Phys. Commun. **77**, 69 (1993).
[48] A. Bödicker, W. Schattke, J. Henk, and R. Feder, J. Phys. Condens. Matter **6**, 1927 (1994).
[49] T. Rauch, M. Flieger, J. Henk, I. Mertig, and A. Ernst, Phys. Rev. Lett. **112**, 016802 (2014).
[50] P. Barone, T. Rauch, D. Di Sante, J. Henk, I. Mertig, and S. Picozzi, Phys. Rev. B **88**, 045207 (2013).
[51] T. Rauch, S. Achilles, J. Henk, and I. Mertig, Phys. Rev. Lett. **114**, 236805 (2015).
[52] J. C. Y. Teo, L. Fu, and C. L. Kane, Phys. Rev. B **78**, 045426 (2008).
[53] H. Wortelen, H. Mirhosseini, K. Miyamoto, A. B. Schmidt, J. Henk, and M. Donath, Phys. Rev. B **91**, 115420 (2015).
[54] S. D. Stolwijk, H. Wortelen, A. B. Schmidt, and M. Donath, Rev. Sci. Instrum. **85**, 013306 (2014).
[55] M. Budke, T. Allmers, M. Donath, and G. Rangelov, Rev. Sci. Instrum. **78**, 113909 (2007).
[56] K. Miyamoto, A. Kimura, T. Okuda, and M. Donath, J. Electron Spectrosc. Relat. Phenom. **201**, 53 (2015).
[57] K. Miyamoto, H. Wortelen, H. Mirhosseini, T. Okuda, A. Kimura, H. Iwasawa, K. Shimada, J. Henk, and M. Donath, Phys. Rev. B **93**, 161403(R) (2016).
[58] A *global* gap separates two bands for all wave vectors $\boldsymbol{k}$; there is a $\boldsymbol{k}$-independent energy range which separates the upper from the lower band. In a *semimetal* gap there is a $\boldsymbol{k}$-dependent energy range separating the two bands.
[59] C. Thiele, K. Dörr, O. Bilani, J. Rödel, and L. Schultz, Phys. Rev. B **75**, 054408 (2007).
[60] S. LaShell, B. A. McDougall, and E. Jensen, Phys. Rev. Lett. **77**, 3419 (1996).
[61] C. R. Ast, J. Henk, A. Ernst, L. Moreschini, M. C. Falub, D. Pacilé, P. Bruno, K. Kern, and M. Grioni, Phys. Rev. Lett. **98**, 186807 (2007).
[62] R. Requist, P. M. Sheverdyaeva, P. Moras, S. K. Mahatha, C. Carbone, and E. Tosatti, Phys. Rev. B **91**, 045432 (2015).
[63] The linear dispersion in W(110) is explained by charge transfer [13].
[64] L.-L. Wang and D. D. Johnson, Phys. Rev. B **83**, 241309 (2011).
[65] M. Franz and L. W. Molenkamp, *Topological Insulators*, edited by E. Burstein, A. H. MacDonald, and P. J. Stiles (Elsevier, Oxford, 2013), Vol. 6.
[66] A. M. Shikin, A. Varykhalov, G. V. Prudnikova, D. Usachov, V. K. Adamchuk, Y. Yamada, J. D. Riley, and O. Rader, Phys. Rev. Lett. **100**, 057601 (2008).
[67] S. V. Chernov, Ultramicroscopy **159**, 453 (2015).
[68] D. Böttcher and J. Henk, J. Phys. Condens. Matter **25**, 136005 (2013).